PROCEEDINGS A

royalsocietypublishing.org/journal/rspa

Research

Check for updates

Cite this article: Amjad K, Lambert P, Middleton CA, Greene RJ, Patterson EA. 2022 A thermal emissions-based real-time monitoring system for *in situ* detection of fatigue cracks. *Proc. R. Soc. A* **478**: 20210796. https://doi.org/10.1098/rspa.2021.0796

Received: 3 December 2021
Accepted: 6 September 2022

Subject Areas:
mechanical engineering

Keywords:
condition monitoring, fatigue, crack monitoring, thermoelastic stress analysis, infrared thermography, microbolometer

Author for correspondence:
K. Amjad
e-mail: khurram.amjad@liverpool.ac.uk

Electronic supplementary material is available online at https://doi.org/10.6084/m9.figshare.c.6214714.

THE ROYAL SOCIETY PUBLISHING

A thermal emissions-based real-time monitoring system for *in situ* detection of fatigue cracks

K. Amjad[1], P. Lambert[1], C. A. Middleton[1], R. J. Greene[2] and E. A. Patterson[1]

[1]School of Engineering, University of Liverpool, Liverpool, UK
[2]Strain Solutions Limited, Chesterfield, UK

KA, 0000-0002-9348-0335; PL, 0000-0001-9525-0667; CAM, 0000-0001-9488-9717; RJG, 0000-0002-5373-0598; EAP, 0000-0003-4397-2160

The advent of packaged infrared (IR) bolometers has led to thermography-based techniques becoming popular for non-destructive evaluation of aerospace structures. In this work, a real-time monitoring system for *in situ* crack detection has been presented which uses an original equipment manufacturer microbolometer. The system costs one-tenth the price of a packaged bolometer and has the potential to transform the use of IR imaging for condition and structural health monitoring in the aerospace industry and elsewhere. A computer, consisting of a single circuit board with dimensions comparable to a credit card, has been integrated into the system for real-time, on-board data processing. Crack detection has been performed based on the principles of thermoelastic stress analysis (TSA). Proof-of-concept laboratory tests were performed on open-hole aluminium specimens to compare the performance of the proposed system against a state-of-the-art cooled IR photovoltaic effect detector. It was demonstrated that cracks as small as 1 mm in length can be detected with loading frequencies as low as 0.3 Hz. This represents a significant advance in the viability of TSA-based crack detection in large-scale structural tests where loading frequencies are usually lower than 1 Hz.

1. Introduction

The aerospace sector is gradually undergoing a paradigm shift with regards to its approach to airframe design and life cycle management. Instead of relying on conservative factors of safety, which has traditionally led to increased structure mass and a higher carbon footprint, the focus has shifted towards designing highly optimized airframes. This dictates the need for the development of compact and reliable structural health monitoring tools for in-service assessment of such optimized structures. Owing to the emergence of cost-effective infrared (IR) cameras over the past decade, IR thermography-based techniques have become popular for non-destructive evaluation (NDE) of aerospace structures [1]. The majority of the IR thermography-based techniques employed for NDE require an external stimulus such as electromagnetic radiation or eddy-currents in order to generate heat in the component under inspection [2]. IR images of the stimulated component are acquired to determine temperature gradients, which are then analysed using various image processing algorithms for the identification of potential defects in the component [2]. Despite being a mature and widely accepted NDE approach, the requirement for an external 'heat source', coupled with the relatively large size of commercially available IR camera systems, renders IR thermography impractical for on-board monitoring of critical locations in a structure under service conditions. This paper focuses on overcoming these major impediments to using an IR thermography-based monitoring system for *in situ* detection of cracks in aerospace structures.

Thermoelastic stress analysis (TSA) is a well-established IR thermography technique, which has been used extensively for quantitative assessment of fatigue cracks in metals [3–5] and damage analysis in composites [6–8]. The working principle of TSA is based on the measurement of small temperature changes associated with the varying stress state in a component resulting from fluctuating applied loads. If the loading rate of a component is significantly higher than the rate of heat transfer to the surrounding material then the observed temperature change, resulting from the thermoelastic effect, is proportional to the change in sum of principal stresses or the first stress invariant [9]. Some of the earliest TSA measurements for determining full-field stress distributions in metallic components under cyclic loading were performed using an IR point-sensor system, e.g. SPATE [10]. These first-generation IR detectors consisted of a single photovoltaic effect sensor, mounted with two independently motorized mirrors, for performing a scan over a component's surface in a point-by-point manner in order to generate a stress map. This time-consuming raster scanning approach hampered the use of TSA for studying time sensitive processes such as fatigue crack propagation. In the 1990s, the advent of IR focal-plane array (FPA) detectors paved the way for TSA to be used in quasi real-time for the evaluation of the stress intensity factor range associated with a fatigue crack, which is considered as the main driving force behind crack propagation [4,11]. These IR detectors essentially consist of a two-dimensional array of photovoltaic effect sensors, which needs to be cooled to cryogenic temperatures (≈77 Kelvin) in order to minimize the internal IR noise of the sensor array.

The application of IR FPA photovoltaic effect detectors for damage analysis in composites using the TSA technique is also well established. Emery & Barton [6] employed TSA to characterize the evolution of fatigue damage resulting from a number of scenarios such as fibre breaking, matrix cracking and inter-layer delamination in fibre-reinforced composite laminates. Opara *et al.* [7] investigated the impact damage in woven fibreglass composite laminates using both the standard TSA technique and pulse heating IR thermography. Their conclusion was that TSA is best-suited to identifying damage resulting predominantly from fibre breakage, whereas inter-layer delamination zones can be observed more clearly with pulse heating IR thermography. The phase difference between the thermoelastic response of a component and the loading signal can also provide meaningful information about the presence of damage. Localized phase shifts are caused by non-adiabatic conditions resulting from nonlinear mechanics, such as plastic deformation in metals or inter-layer delamination in composites. This phase information has been successfully used in the past to estimate fatigue life [12] and determine the size of the crack tip plastic zone [3,13] in metals. It has also been used for monitoring damage evolution in composite materials [14,15].

It is evident from reviewing the literature on TSA that the IR FPA photovoltaic effect detectors significantly enhanced the practical appeal of the TSA technique in the first two decades after their development. However, the utility of TSA in industrial environments has lagged behind other, more-widely accepted, full-field strain measurement techniques such as digital image correlation (DIC). One of the major reasons for this is the high capital cost of the IR FPA photovoltaic effect detectors. Also, their size and mass are significantly greater compared to the imaging technology typically employed in other full-field strain measurement techniques. This issue has been addressed to some extent by the commercial availability of microbolometers in the past decade, which are an order of magnitude cheaper than the IR FPA photovoltaic effect detectors. Microbolometers consist of an array of IR absorptive elements with a temperature-dependent electrical resistance. The change in electrical resistance generates an electrical signal which can be calibrated to perform temperature measurements.

The temperature resolution of an IR detector is typically defined in terms of the noise equivalent temperature difference (NETD), which is essentially a minimum temperature change that an IR detector can resolve. Modern IR FPA photovoltaic effect detectors have an NETD in the range of 10–20 mK [16]. This translates to a stress change of 4–8 MPa in aluminium. However, the stress sensitivity of TSA is not necessarily limited by the NEDT of an IR detector [17]. In TSA, signal processing is employed to extract temperature fluctuations associated with the thermoelastic effect, as low as 1 mK, from the raw IR data. This results in a stress sensitivity for TSA on the order of 1 MPa [16]. Rajic & Street [17] carried out a comprehensive study to demonstrate that a microbolometer with an NETD of 120 mK can be effectively used for quantitative analysis using the TSA technique, which was previously believed to be possible only with the high-specification IR FPA photovoltaic effect detectors. The wide-spread availability of low-cost bolometers has undoubtedly improved the feasibility of TSA for use in industrial environments. There have been a few recent studies in which microbolometers were used for stress analysis on aerospace [18] and civil [19] structures using the TSA technique. Despite these recent advances, TSA is still perceived as a stress analysis technique which is difficult to employ outside of a controlled laboratory environment. Its potential use in structural health monitoring applications has, therefore, still not been fully explored.

To the best of the authors' knowledge, all of the previously published studies on low-cost TSA employed industrial-grade 'packaged' bolometers which consisted of an IR sensor array, associated electronics and the optical arrangement all packaged inside a protective housing. These packaged bolometers are typically controlled through their dedicated commercial software modules which are compatible with either Microsoft Windows, Macintosh or the Linux operating systems, and hence, require a user-controlled desktop or a laptop computer to operate. It is, therefore, difficult to deploy them in inaccessible or hard-to-reach locations in a structure or where there are restrictions on weight, volume and availability of power, e.g. in an aircraft during flight operations. Recent work by some of the current authors has demonstrated the potential for the original equipment manufacturer (OEM) microbolometers to be used for monitoring cracks under constant amplitude sinusoidal loading [20]. In this work by Middleton *et al*. [20], IR responses to constant amplitude sinusoidal loading were captured using an OEM microbolometer. The acquired data was post-processed to show the crack propagation detection capability of such low-cost bolometers. OEM microbolometers are available at one-tenth of the price of packaged bolometers and can be controlled through a computer consisting of a single circuit board with dimensions comparable to a credit card [20]. This paper reports the development of a compact, low-cost system, which uses an OEM microbolometer for quasi real-time detection and monitoring of fatigue cracks based on the principles of TSA. The system was designed with the aim of advancing the feasibility of *in situ* crack monitoring at critical locations in large-scale structures, under realistic loading conditions. Proof-of-concept laboratory tests were performed on open-hole aluminium specimens, subjected to uniaxial flight cycle loading

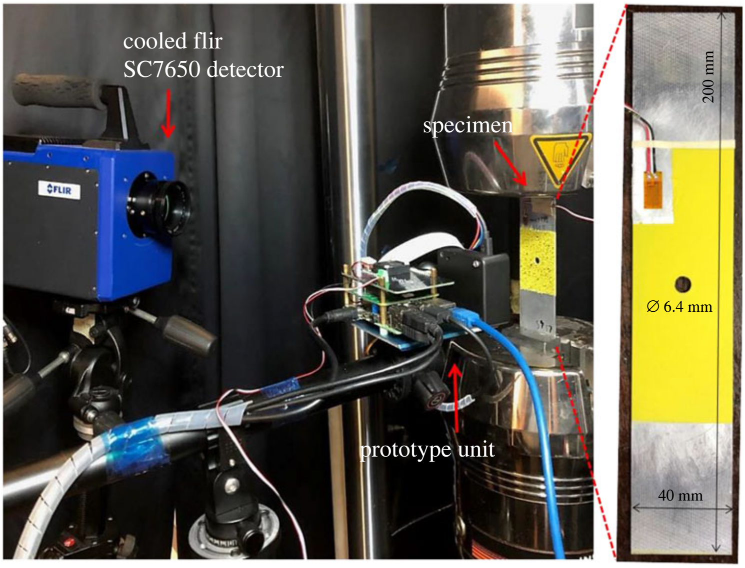

Figure 1. Photographs of the experimental set-up showing the prototype unit for real-time crack monitoring, cooled Flir SC7650 detector used for comparing the crack detection capability of the prototype unit and the open-hole aluminium specimen. Additional photograph of the prototype unit showing all its components is provided in electronic supplementary material, figure S4. (Online version in colour.)

involving frequencies of the order of 1 Hz, to establish its crack monitoring performance against the state-of-the-art cooled photovoltaic effect detector.

This paper is structured in the following manner: the next section provides a description of the TSA theory and the proposed TSA-based crack detection method. The description of the prototype unit for real-time fatigue crack monitoring is provided in the third section. Detailed description of the three proof-of-concept fatigue tests, performed to establish the crack monitoring capability of the prototype unit, can also be found in this section. The experimental set-up for these tests is shown in figure 1. Results of the three fatigue tests are analysed and discussed in the fourth section. The loading frequency and the strain amplitude ranges over which the prototype system can perform crack detection are also discussed in this section. The key findings of this study and concluding remarks are provided in the final section.

2. Proposed crack detection method

(a) Thermoelastic stress analysis

As discussed in the previous section, TSA is primarily a quantitative stress analysis technique which is applied, predominantly, for determining the stress distribution in components under constant amplitude cyclic loading. Detailed mathematical formulations underpinning the theory of TSA can be found in a review paper by Pitarresi & Patterson [9]. For an isotropic material in a state of plane stress under adiabatic conditions, the temperature change resulting from the thermoelastic effect is related to the change in the sum of stresses using the following equation:

$$\Delta T = -\frac{\alpha T}{\rho C_p}\Delta(\sigma_{11} + \sigma_{22}), \tag{2.1}$$

where ΔT is the temperature change, T is the absolute temperature, α is the coefficient of linear thermal expansion, ρ is the density, C_p is the specific heat capacity at constant pressure, and σ_{11}

and σ_{22} are the in-plane maximum and minimum principal stresses, respectively. The relation typically employed for practical TSA is as follows:

$$AS = \Delta(\sigma_{11} + \sigma_{22}), \tag{2.2}$$

where S is the signal from an IR detector and A is the calibration constant, which is a function of the IR detector parameters and the properties of the material being inspected. The value of the calibration constant is typically determined experimentally by obtaining the detector signal from a region on the component's surface with a known stress state.

The above relations are only valid if adiabatic conditions are met. The loading rate required to ensure quasi-adiabatic conditions not only depends on the material properties but also on the stress gradients in a component, which are a function of both the component's geometry and the magnitude of applied loads. To ensure the thermoelastic effect is acquired under quasi-adiabatic conditions, a typical rule-of-thumb is to perform cyclic loading at a frequency of at least 10 Hz [21]. However, it has been demonstrated that loading frequencies as high as 30 Hz are required to resolve elastic stresses around a crack tip in aluminium [22]. This stringent requirement on the loading rate makes TSA challenging to employ for fatigue assessment in large-scale structural tests where the loading frequencies are usually quite low, i.e. less than 1 Hz [18].

The above TSA equations essentially dictate a linear relationship between the applied stress amplitude in the material and its thermoelastic response under adiabatic conditions. More complex theoretical relationships for TSA have been derived in the past, which consider the influence of both the temperature variation in the material during load cycle and the mean stress on the thermoelastic response as well [9,23]. In practice, it is not uncommon to ignore the 'negligible' influence of these two factors and assume a linear relationship between the applied stress amplitude and acquired thermoelastic response from a component's surface. However, it has been demonstrated experimentally that the influence of these factors on the thermoelastic response is not negligible in certain materials, e.g. aluminium and titanium [24]. The focus of the current work is developing a methodology for detecting a change in condition caused by the initiation or growth of a crack rather than quantitative stress analysis. This is achieved by determining changes to the spatial distribution of thermoelastic response from a component's surface under fatigue loading. Hence, the analysis is performed using an un-calibrated detector signal (S), which represents temperature fluctuations caused predominantly by the thermoelastic effect under both quasi-adiabatic and non-adiabatic conditions. To avoid confusion with the conventional TSA approach for quantitative measurement of stresses, the analysis reported in the work is, therefore, referred to as Condition Assessment using Thermal Emissions (CATE).

The proposed method can be divided into two parts. The first part involves the acquisition of data from the OEM microbolometer and an electrical resistance strain gauge (RSG), which is bonded on to the component under inspection. The acquired data is processed in quasi real-time to generate a spatial map of the un-calibrated detector signal (S), which will hereon be referred to as the 'CATE' map. In the second part, these CATE maps are further processed for automated tracking of fatigue cracks. The two parts of the method are described in the subsections below and in detailed flow charts provided in electronic supplementary material, figures S1 and S2.

(b) Data acquisition and processing

The method for crack detection is designed for both constant amplitude cyclic loading and flight cycle loading. An idealized flight cycle [20], representing different events during take-off, cruise, gust loading, landing and taxiing in a typical flight operation, is shown in figure 2. In this method, the spatial IR data from an OEM microbolometer and the RSG point data are acquired simultaneously over an operator-defined time window. The acquired RSG signal is then processed to identify distinct waveforms in the loading block without *a priori* knowledge of the applied loading. This process involves evaluating the local gradient at each point in order to first identify all the peaks and troughs in the RSG signal. Each pair of adjacent peaks within the RSG signal is then interrogated to determine the frequency, to a resolution of 0.01 Hz, and amplitude, to a

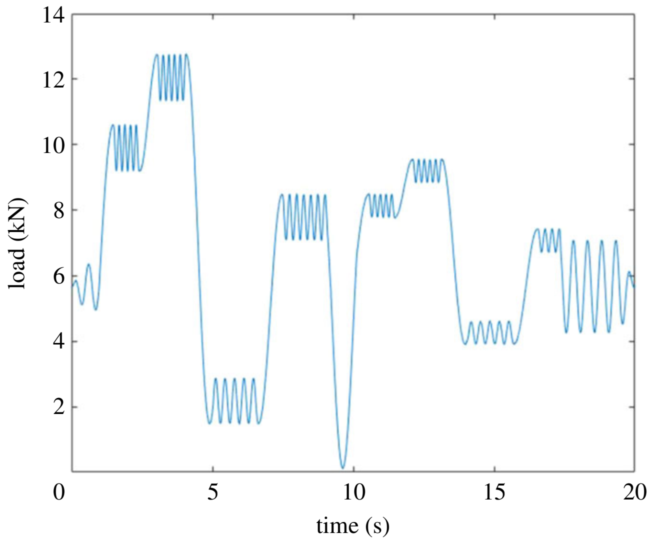

Figure 2. Idealized flight cycle [20] comprised of distinct waveforms which represent different events during take-off, cruise, gust loading, landing and taxiing in a typical flight operation. (Online version in colour.)

resolution of 2 $\mu\varepsilon$, of an underlying signal component connecting them. The next step is to map the components of the RSG signal in to the frequency–amplitude domain defined between 0.05–3 Hz and 100–1000 $\mu\varepsilon$. This frequency range is representative of the frequencies usually involved in fatigue testing of aircraft sub-assemblies, whereas, the range of strain amplitude lies within the fatigue endurance limit and the yield strain of a typical aerospace-grade aluminium alloy. This results in clusters of points in the frequency–amplitude domain that each represent a distinct waveform within the RSG signal and were automatically detected using the image processing operations of morphological closing [25] and connected-region labelling [25] performed by standard functions from an open-source computer vision library (OpenCV, Intel corporation, USA). Figure 3 shows the resultant 13 distinct waveforms which were identified in the flight cycle, provided in figure 2.

To extract the thermoelastic response resulting from each distinct waveform, the signal components in a given cluster are first stitched together to construct a reference signal. Time stamps of the RSG values from the reference signal are then used to retrieve IR images corresponding most closely to these times. The retrieved IR images are formed into a volumetric array such that the images are the x-y planes with time represented by the z-dimension. Finally, a CATE map for each distinct waveform is extracted from raw IR data by fitting the reference signal to the temporal IR distribution at each pixel location in the x-y plane of the volumetric array using the least-squares method. The CATE map represents the spatial distribution of the thermoelastic signal amplitude resulting from that particular or distinct waveform. Figure 4 shows the exemplar CATE maps derived from the 13 distinct waveforms identified in the flight cycle shown in figure 2 using a time window of 150 s corresponding to 7.5 repetitions of the flight cycle. An additional CATE map for the whole flight cycle is also provided in figure 4. This CATE map represents the 'broadband' thermoelastic response resulting from the combined effect of all the waveforms constituting the flight cycle and is produced by simply fitting the un-processed RSG signal to the raw IR data, acquired over several flight cycles, using the least-squares approach.

(c) Crack tracking

An image-based decomposition technique based on discrete orthogonal polynomials [26,27] is used for automated tracking of fatigue cracks from the CATE maps. This technique is

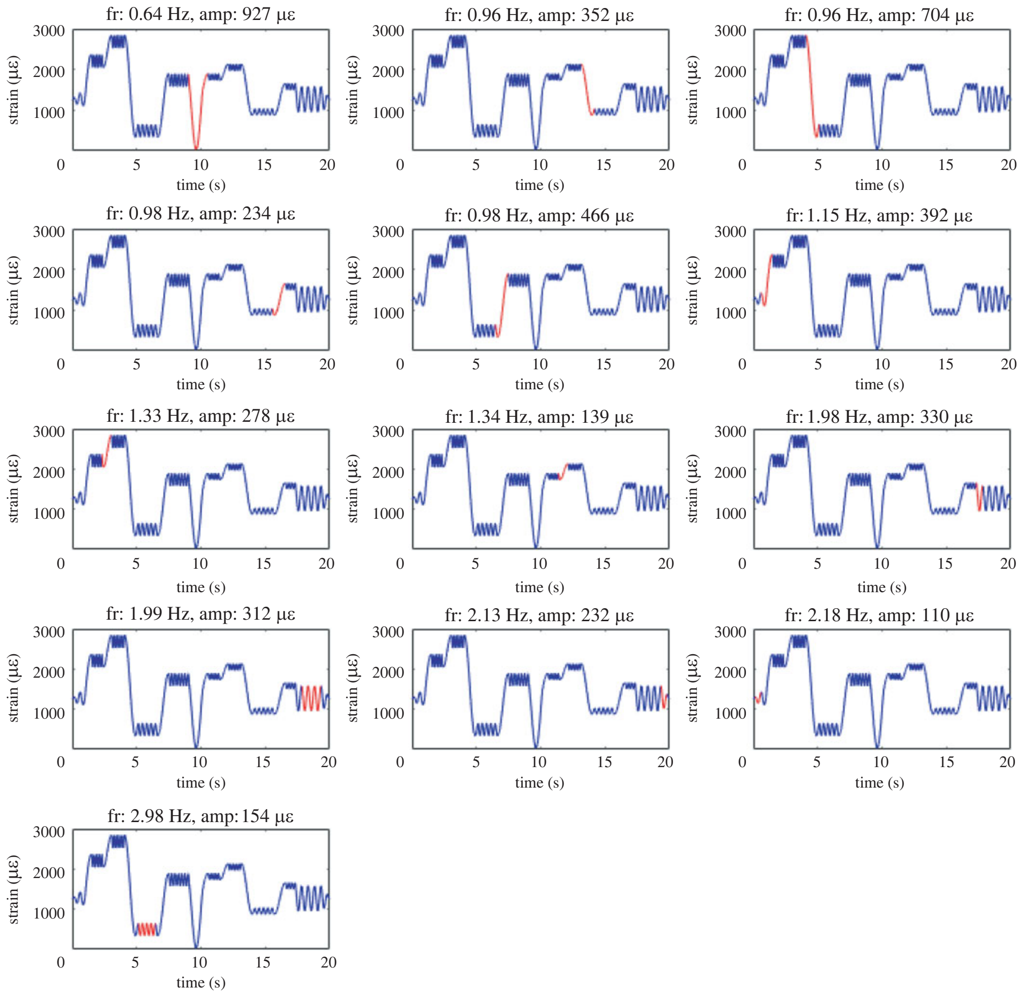

Figure 3. Distinct waveforms (red) identified in the idealized flight cycle (blue) are shown in figure 2. This figure can be interpreted in colour only. (Online version in colour.)

well-established for quantitative comparisons of data fields [28], including tracking of damage [20,29], and treats strain fields as digital images that are decomposed by fitting a pre-defined set of two-dimensional polynomial kernels to the intensity distribution of the image. The coefficients of the fitted kernels are collated into a column vector, often referred to as a feature vector, which provides a unique representation of the data field in the image. In the proposed method, each CATE map is decomposed to a feature vector using kernels described by discrete Chebyshev polynomials so that the feature vector represents the spatial distribution of the thermoelastic signal resulting from a distinct waveform of loading. The first coefficient in the feature vector belongs to the zero-order polynomial kernel, and hence, is indicative of the mean thermoelastic amplitude. The initiation or propagation of a crack would induce a change in the spatial distribution of thermoelastic amplitude over a component's surface, and hence, also in the feature vector for the CATE map. The change in the feature vector is evaluated by calculating the Euclidean distance between vectors representing the current state and a reference state acquired at the beginning of the test, which represents the 'un-damaged' state of the component. It is important to highlight here that the first coefficient of feature vectors, representing the mean thermoelastic response, is excluded from Euclidean distance calculation in order to filter out the effect of factors, such as temperature drifts, which could potentially cause the mean thermoelastic

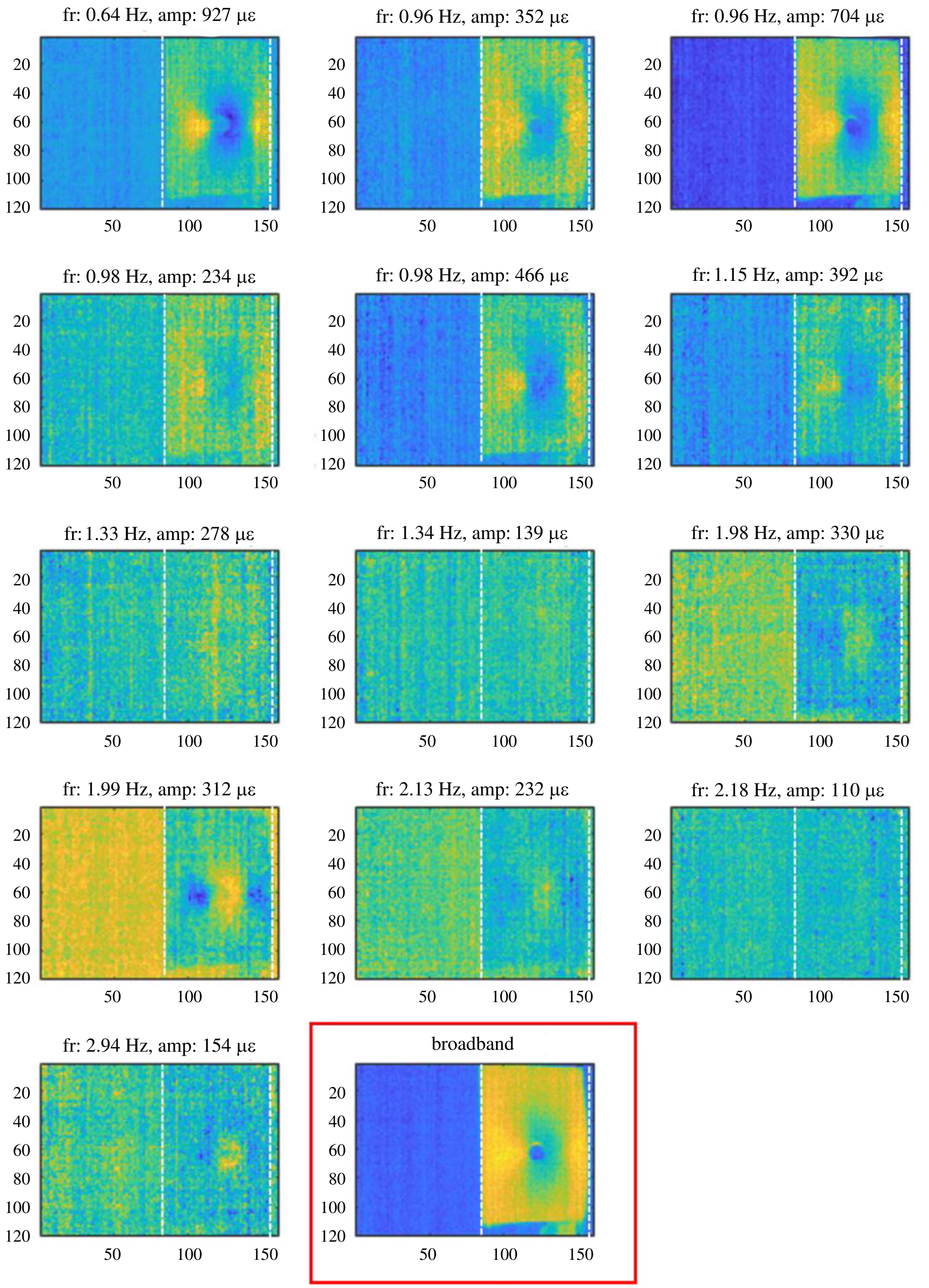

Figure 4. Exemplar normalized CATE maps representing thermoelastic response caused by the distinct loading waveforms shown in figure 3. The extra CATE map in the last row, highlighted with a box, represents the broadband thermoelastic response resulting from the combined effect of the waveforms comprising the idealized cycle. Dashed white lines in the CATE maps highlight the specimen edges in the Lepton microbolometer field-of-view. Numbers on axes are image pixel values. (Online version in colour.)

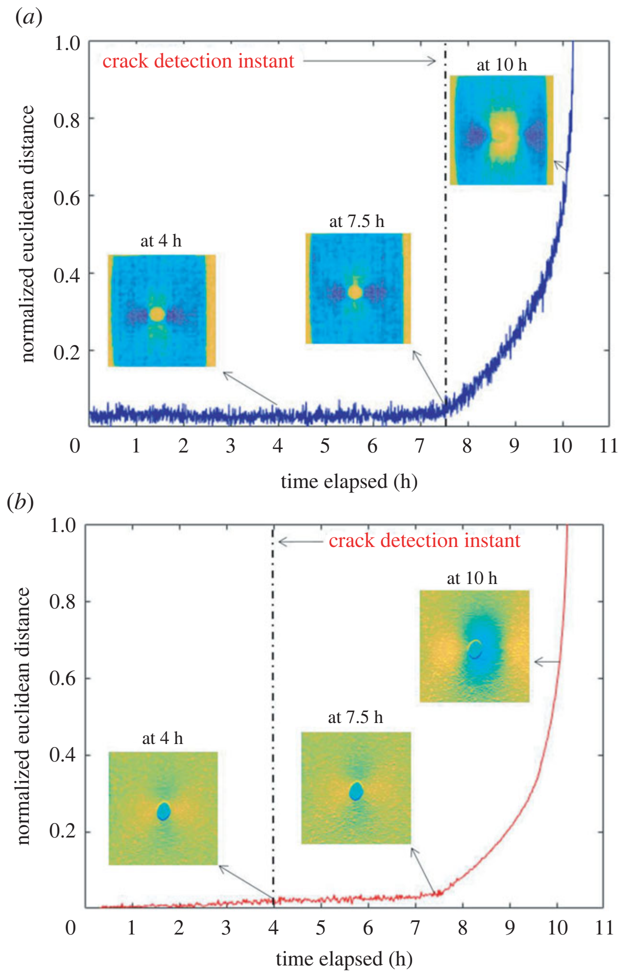

Figure 5. Plots of normalized Euclidean distance against time for constant amplitude sinusoidal loading in Test 1 (table 1) produced using the prototype unit using quasi real-time processing (*a*) and cooled IR photovoltaic effect detector with post-processing of data (*b*). Insets show the corresponding CATE maps at three different times during fatigue loading; the change in the maps indicates that cracks grow horizontally from the points on the edge of the hole which are furthest from the vertical axis of loading. (Online version in colour.)

response to change or drift over the course of a fatigue test. In the proposed method, the evolution of Euclidean distance over time for each distinct waveform identified in the flight cycle is plotted in quasi real-time.

(d) Post-processing

Middleton *et al.* [20], using a similar OEM microbolometer, have shown that a significant increase in the Euclidean distance from a baseline provided a clear indication of crack propagation. An equivalent example of the evolution of Euclidean distance over time is shown in the top plot of figure 5 for an open-hole aluminium specimen under constant amplitude sinusoidal loading. Detailed description of this test and the specimen is provided in §3. The baseline value for the Euclidean distance was established for the top plot in figure 5 by calculating its mean, median and standard deviation over the initial 2 h of loading. A rolling median of the Euclidean distance was then calculated using a window length of 11 data points. The instant of crack detection was defined to be where the difference between the rolling median and the baseline median

Table 1. Summary of the fatigue tests performed in this experimental study. During the course of each fatigue test, raw IR and RSG data were recorded continuously in batches over the pre-defined time window reported in the fifth column of the table.

<table>
<tr><th>test no.</th><th>data acquisition system</th><th>loading prior to data capture</th><th>loading during data capture</th><th>data capture window (s)</th></tr>
<tr><td>1</td><td>cooled photovoltaic effect detector and prototype unit</td><td>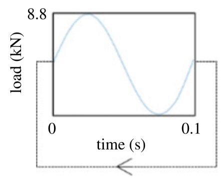

80 000 cycles</td><td>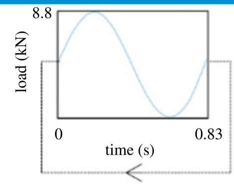

44 064 cycles at specimen failure</td><td>cooled photovoltaic effect detector: 4, prototype unit: 16</td></tr>
<tr><td>2</td><td>prototype unit</td><td>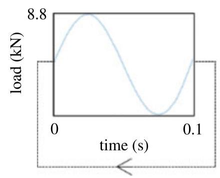

80 000 cycles</td><td>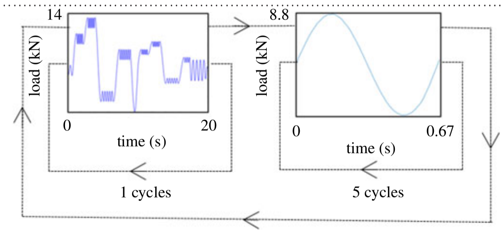

5687 cycles until specimen failure</td><td>250</td></tr>
<tr><td>3</td><td>prototype unit</td><td>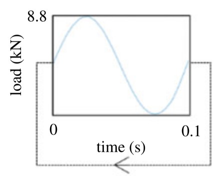

80 000 cycles</td><td>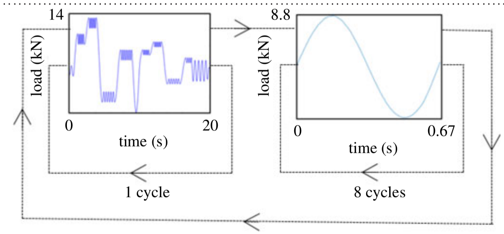

4400 cycles until specimen failure</td><td>450</td></tr>
</table>

permanently exceeded the standard deviation of the baseline mean which happened after 7.5 h. The rolling median is used instead of the rolling mean because it is more robust to outliers in the data [30]. A significant advantage of this method is that it is entirely possible to perform this simple statistical analysis in quasi real-time, in order to generate an alert for the test operator indicating the presence of damage or a fatigue crack. The effect of the initial time window for establishing the baseline Euclidean distance value and the window length for evaluating the rolling median of the Euclidean distance is shown in electronic supplementary material, figure S3.

3. Experimental method

A prototype unit, shown in figure 1, was developed which used an OEM microbolometer (Lepton 3, FLIR, Wilsonville, OR, USA) with a sensor array of 160×120 pixels, an NEDT of 50 mK and an IR spectral range of 8–14 µm. The detector is capable of capturing IR images with an effective frame rate of 8.8 Hz. It was controlled using a Raspberry Pi 4 (Raspberry Pi Foundation, UK), which is a single board computer of dimensions $85 \times 56 \times 17$ mm and is ideal for on-board data processing. An additional power-over-Ethernet board was used to power the Raspberry Pi through an Ethernet cable. A quarter Wheatstone bridge (WSB) circuit was also incorporated, which was powered by a 3.3 V supply from the Raspberry Pi computer. The purpose of this WSB was to process the signal from an 'active' RSG, bonded onto the structure or component under inspection, in order to measure local strain levels resulting from the applied loads. A 16-bit analogue-to-digital converter (ADC) was used to digitize the differential analogue input from the WSB circuit at a sampling rate of 158 Hz. The digitized output from the ADC was read out through the digital input channel of the Raspberry Pi computer. The prototype unit also included a visible light imaging system which allowed visual inspection of the area of interest. This consisted of an 8 mega-pixel image sensor (IMX219, Sony Corporation, Japan) with a circular array of 16 programmable LED lights around the image sensor. As the title suggests, this paper is focused on demonstrating crack detection capability based on thermal emissions, and hence, any data acquired using the visible-light imaging system are neither reported nor discussed here. The computer script implementing the proposed method for crack detection, described in the previous section, was written in Python for execution on the Raspberry Pi computer. Electronic supplementary material, figure S4 provides a comparison of the size, weight and cost of the prototype unit with that of a state-of-the-art cooled IR photovoltaic effect detector (FLIR SC7650, Teledyne FLIR LLC, USA). Proof-of-concept tests were performed on aluminium specimens to establish the capabilities of the prototype unit and the proposed crack detection method.

Rectangular specimens of dimensions 200×40 mm were machined from a 1.6 mm thick aluminium 2024-T3 sheet. A central hole of 6.4 mm diameter was drilled in each of the specimens, this hole acts as a stress concentrator during fatigue loading, so that fatigue cracks will grow from the hole edges. For TSA measurements, the specimen is usually painted with a non-reflective matt-black paint in order to reduce background IR reflections and ensure uniform and high emissivity over the specimen's surface. In this work, the specimen was instead painted with an aviation primer (LAS780-001, LAS Aerospace Ltd, UK) that is commonly used on aerospace structures for protection against corrosion. Prior work has shown that similar primer paint provides a uniform and high emissivity [31]. It is a common practice in large-scale industrial tests to employ different NDE techniques to assess critical locations in a structure. One such widely used non-contact optical technique is DIC, which requires creation of a random speckle pattern over the region of interest. Hence, the base coat of yellow-coloured aviation primer on each specimen's surface was speckled with random black dots using a spray paint (Acrylic paint, CRC Industries Europe, Belgium) to represent surface preparation likely to be encountered in an industrial test. The speckles are not visible in the raw IR images or the processed CATE maps acquired from the Lepton microbolometer, as demonstrated in electronic supplementary material, figure S5. It was, therefore, assumed that these speckles did not affect the crack detection results.

A 350 Ω RSG (CEA-13-250UW-350, Vishay Intertechnology Inc., USA) was bonded onto each specimen, away from the hole edge and out of the field of view of the IR and visible light system, and was used to measure nominal strain levels in the specimen under loading i.e. to process the RSG signal described in §2.2. A synthetic reference can be generated from raw IR data acquired at frequencies typically used in quantitative TSA, i.e. above 10 Hz; however, for low-frequency waveforms inducing low strain amplitudes in the material, a reference signal from an external source, such as a strain gauge, is a requirement to provide a good signal-to-noise ratio.

In total, three fatigue tests were performed. To accelerate the crack initiation stage, each of the three specimens was initially loaded for 80 000 sinusoidal cycles at 10 Hz using a maximum load of 8.75 kN and a load ratio of 0.1. For the first test, constant amplitude sinusoidal loading was continued after switching the loading frequency to 1.2 Hz until failure of the specimen. For the other two tests, the loading regime was switched to a spectrum of loading representative of a flight cycle. The load sequence in the second test was comprised of a flight cycle, shown in figure 2, followed by five cycles of sinusoidal loading at 1.5 Hz. This sequence was repeated continuously until specimen failure. The load sequence for the third test used the same flight cycle in figure 2; however, its time period was stretched to 40 s in order to reduce the frequencies of the signal components in the flight cycle and test the capabilities of the CATE method. The stretched flight cycle was followed by eight cycles of sinusoidal loading at 1.5 Hz in the third test. The loading details of the three fatigue tests are summarized in table 1.

For the two tests involving flight cycle loading, the data were acquired using the prototype system; however, for the first test, the data were captured simultaneously using the prototype system and, for comparison, a high-resolution and high-sensitivity cooled IR detector (FLIR SC7650, Teledyne FLIR LLC, USA) consisting of an array of 640×512 photovoltaic effect sensors and fitted with a 50 mm IR lens. The cooled photovoltaic effect detector was placed at a stand-off distance of 400 mm and a viewing angle of about 45° from the specimen surface providing a spatial resolution of 0.2 mm pixel^{-1}. The camera unit was integrated with the DeltaTherm acquisition system (Stress Photonics, USA), which acquires and processes the IR data stream from the photovoltaic effect detector in quasi real-time in order to produce un-calibrated TSA (CATE) maps. These maps were produced continuously by capturing the IR image stream every four seconds, at a frame rate of 328 Hz, with an active sensor window of 320×256 pixels. The acquired CATE maps from the DeltaTherm system were imported into a specially written MATLAB program for post-processing and subsequently decomposed into feature vectors to produce a plot of Euclidean distance against time. The prototype unit was placed at a stand-off distance of 75 mm with the Lepton sensor aligned parallel to the specimen surface, thereby, providing a spatial resolution of 0.6 mm pixel^{-1}. It was not physically possible to match the spatial resolution of the prototype unit to that of the photovoltaic effect detector, i.e. 0.2 mm pixel^{-1}, as this would have required a stand-off distance of 24 mm. The raw RSG and IR data were recorded continuously in batches over windows of 16, 250 and 450 s for the three tests, respectively and processed in quasi real-time to generate Euclidean distance values for each distinct waveform in the loading sequence throughout the test duration.

4. Results and discussion

The values of normalized Euclidean distance from both the cooled photovoltaic effect detector and the prototype unit are plotted against time in figure 5 for the constant amplitude sinusoidal loading in Test 1. The characteristic localized hot spot at the crack tip cannot be observed in the relatively high-resolution CATE maps from the photovoltaic effect detector (see insets figure 5) because the loading frequency of 1.2 Hz was an order of magnitude lower than required to ensure adiabatic conditions in aluminium. The heat conduction at such low loading frequency caused the hot spots to appear blurred and diffuse. All the previously published TSA-based methods [4,32–34] for tracking crack growth rely on the presence of a well-defined localized hot-spot at a crack tip, which is typically distinguishable at a loading frequency in excess of 10 Hz. This limits the applicability of these methods in fatigue assessment of large-scale structures where the loading frequencies are often of the order of 1 Hz [18]. By contrast, the image decomposition-based approach, used in this work, quantifies subtle changes to the global shape of the CATE maps, which are caused by the initiation or propagation of a fatigue crack. Hence, this approach is capable of tracking crack propagation from the thermoelastic response, acquired under non-adiabatic conditions, at low loading frequencies as demonstrated by the results in figure 5. One limitation of the feature vector approach for crack tracking is that it does not provide direct measurement of crack length, which is required for making fatigue life estimates of a component. There is the potential for establishing a relationship between increases in the Euclidean distance between feature vectors representing the CATE maps at different stages of the crack growth and the extension of the crack in order to make an estimate of fatigue life; however, this is beyond the scope of this study.

The instants at which a permanent significant increase in the Euclidean distance relative to its baseline value were found, using the method described in §2.4, to be 4 and 7.5 h for the cooled photovoltaic effect detector and the prototype unit, respectively. It has been established from previous fatigue studies [13,20,33] on similar open-hole aluminium alloy specimens that the FLIR IR photovoltaic effect detector is capable of detecting a sub-millimetre crack. There is a linear increase in the Euclidean distance between 4 and 7.5 h in the plot for the photovoltaic effect detector (figure 5), which indicates the initiation and extension of a short crack causing a change in the elastic stress field. The rate of change in the Euclidean distance starts to increase after 7.5 h which is indicative of crack propagation. At the same time, there is an increase in the Euclidean distance based on the data from the prototype system, which implies that the prototype system was able to detect the presence of a crack at the onset of the crack propagation stage. A naturally initiated crack, originating from the hole edge for this specimen geometry, is in the range of 1–2 mm in length at the onset of the crack propagation stage [13,20], which implies that the prototype system can detect cracks in this length range. Discussion with some sectors of the aerospace industry has implied that the existing inspection methods employed during aircraft maintenance are typically capable of detecting cracks when they are about 10 mm in length. Hence, the hardware and software solution proposed in this paper offers a huge potential for early detection of fatigue cracks and optimization of maintenance intervals.

The loading sequences used in Tests 2 and 3 were comprised of two segments: (1) flight cycle loading and (2) constant amplitude sinusoidal loading. The primary purpose of the latter segment was to insert a waveform into the loading sequence which would induce a strong thermoelastic response from the specimen and whose Euclidean distance curve could be used as a benchmark for comparison with those resulting from the waveforms identified in the flight cycle segment. The latter segment also helped to achieve crack propagation on a more feasible timescale in these laboratory tests. In total, 16 and 17 distinct waveforms, respectively, were detected within the pre-defined frequency range of 0.05–3 Hz in the loading sequences of Test 2 and Test 3. CATE maps from each of the identified loading waveforms were produced and subsequently decomposed into feature vectors in quasi real-time throughout the loading duration in both the tests. The Euclidean distances between feature vectors were calculated and plotted against time for each waveform. Figure 6 shows the Euclidean distance plots, produced in quasi real-time, for the identified waveforms in the loading sequence for Test 2 and the corresponding set of similar plots for Test 3 are given in electronic supplementary material, figure S6. There are additional Euclidean distance plots, highlighted in a box in both figures, which represent the change in the broadband thermoelastic response from the flight cycle loading segment. As mentioned in an earlier section, the prototype system was intended to work primarily with two loading regimes, i.e. constant amplitude cyclic loading and flight cycle loading. However, by determining a 'broadband' thermoelastic response, it is possible to employ the system for tracking cracks induced by a non-repetitive, random loading regime as well. The CATE map representing broadband thermoelastic response is determined by correlating the RSG signal with the IR images acquired over a user-specified time period resulting in those components in the RSG signal which do not generate a significant thermoelastic response being filtered out. Hence, the broadband CATE map represents the combined thermoelastic effect from significant loading events during the acquisition interval. The Euclidean distance plots for broadband CATE maps in both figure 6

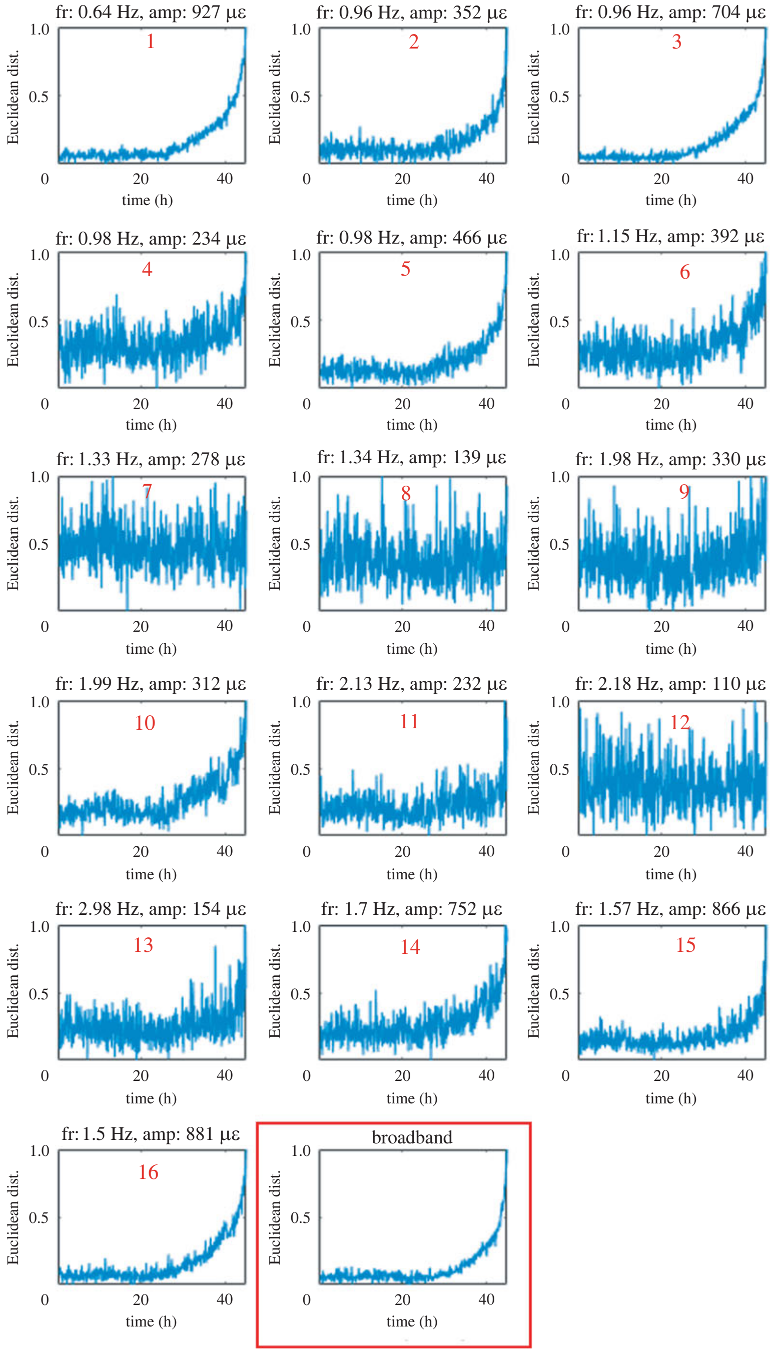

Figure 6. Plots of normalized Euclidean distance against time for the 16 distinct waveforms detected in the Test 2 loading sequence described in table 1. The first 13 plots correspond to the 13 distinct waveforms, shown in figure 3, which constitute the idealized (un-stretched) flight cycle in figure 2. Plot 16 corresponds to the constant-amplitude sinusoidal waveform whereas plots 14 and 15 are linked to the waveforms, which arise from the ramp components used for linking the two loading regimes together in the Test 2 loading sequence. The extra plot in the last row, highlighted with a box, represents the change in 'broadband' CATE maps resulting from the whole un-stretched flight cycle in the Test 2 loading sequence.

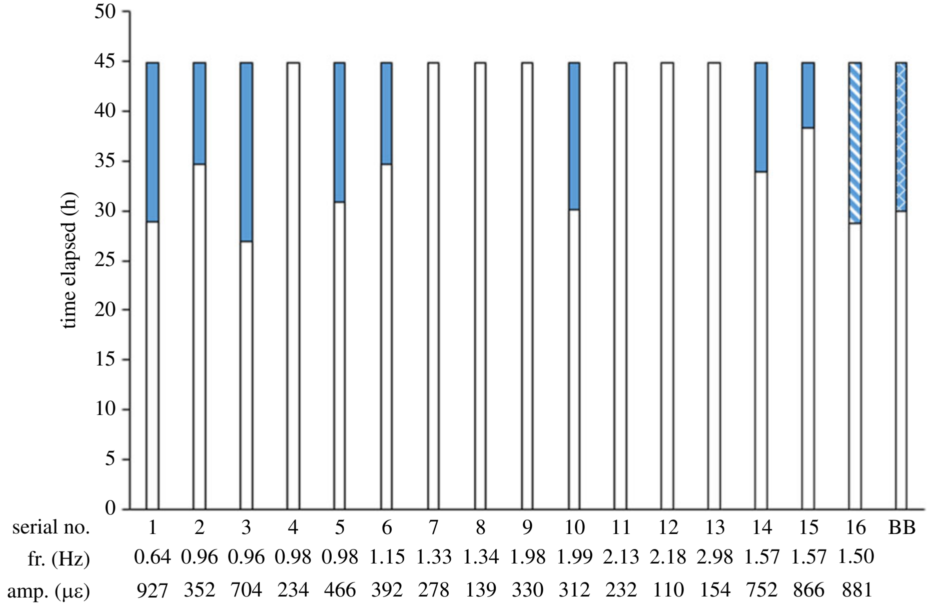

Figure 7. Bar chart illustrating crack detection times based on Euclidean distance plots in figure 6 for Test 2 (table 1). Un-filled sections of the bars represent time duration over which no crack was detected. Filled sections represent the time duration over which a propagating crack was detected. Bars with diagonal and diamond-filled patterns belong to the 'benchmark' constant amplitude sinusoidal waveform and the whole flight cycle in the loading sequence, respectively. BB indicates broadband cycle. (Online version in colour.)

and electronic supplementary material, figure S6 exhibit a characteristic shape of an exponential growth curve, which is indicative of crack propagation.

Some of the plots in figure 6 have the characteristic profile of an exponential growth curve while there is no discernible trend in others, which indicates that the prototype system was not sensitive to the thermoelastic response caused by the loading waveforms associated with these latter plots. To identify the loading waveforms which can be used for crack detection, instants of crack detection were determined for each of them, using the statistical approach described in §2.4. These crack detection instants are illustrated using a bar chart in figure 7 for Test 2 and electronic supplementary material, figure S7 for Test 3. The bar height represents the whole loading duration of the test, the shaded section shows the time period over which a significant change in the thermoelastic response has been detected and their interface indicates the instant of crack detection. In Test 2, there are two Euclidean distance curves, associated with waveforms 1 and 3, whose instant of crack detection are either earlier or at approximately the same time as that for the benchmark Euclidean distance curve (see diagonal shaded bar in figure 7). This implies that a strong thermoelastic response was being generated from these loading waveforms in the flight cycle. Under adiabatic conditions, the thermoelastic response around a crack tip is proportional to the range of the stress intensity factor which is indicative of the crack driving force. Hence, it is postulated that the two identified waveforms had likely contributed to crack initiation and propagation. This type of analysis would not only allow identification of the load events which are critical to loss of structural integrity but is also likely to be significant in improving fatigue life prediction models.

Test 3 was performed to investigate the effect of reducing the loading frequency on the crack detection capability of the prototype system. This was achieved by increasing the time period of the original flight cycle in figure 2 from 20 to 40 s. The reduction in the loading rate causes the surface temperature changes generated by the thermoelastic effect to dissipate within the material, which results in a weaker IR signal reaching the sensor array. Unlike Test 2, there

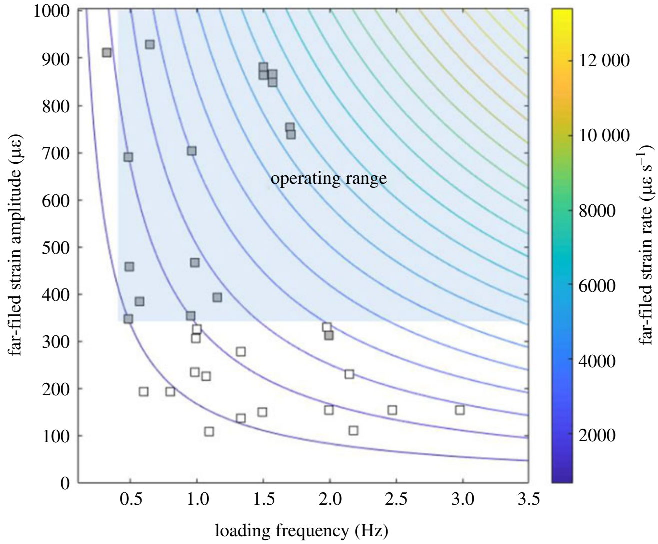

Figure 8. Scatter plot of the waveform amplitudes and frequencies identified using the analysis described in §2.2. Filled squares represent those waveforms whose Euclidean distance curves registered a significant thermoelastic response to allow crack detection, whereas the unfilled squares represent those loading waveforms which did not induce significant thermoelastic response from the specimen. A set of contour curves show the lines of constant nominal strain amplitude in the specimen. The shaded region of the plot highlights the operating range of the proposed system for aluminium alloy material. (Online version in colour.)

was no loading waveform in the stretched flight cycle of Test 3 for which the instant of crack detection occurred prior to that of the benchmark loading waveform. This signifies the adverse effect of the reduced loading frequency on the system's crack detection capability. The range of loading frequencies and nominal strain levels, over which the prototype system was able to perform crack detection, were explored by plotting in figure 8 the waveform frequencies and amplitudes obtained from Tests 2 and 3 using the analysis described in §2.2. The data points for those loading waveforms whose Euclidean distance curves registered a significant change in thermoelastic response using the rolling median approach described in §2.4, indicating the presence of a crack, are plotted with filled squares and are found in the upper two-thirds of the graph. On the other hand, the un-filled squares represent those waveforms which did not generate a significant thermoelastic response in this study and located in the lower third of the graph. Hence, this scatter plot defines the limits of the capabilities of the new method and can be used to identify the lower limits for the frequency and nominal strain amplitude required in a loading waveform that would ensure a significant thermoelastic response and allow crack detection with the prototype system. Interestingly, the lower bounds for strain amplitude and frequency do not follow one of the contour lines of constant nominal strain rate. The factor which seems to be dictating the lower bound is the nominal strain amplitude. There is a cut-off strain amplitude of about 350 με, equivalent to 25 MPa in aluminium, below which loading waveforms did not generate a significant thermoelastic effect to allow crack detection, irrespective of their frequency. The plot also reveals that crack detection is possible with loading frequencies as low as 0.3 Hz if the nominal strain amplitudes are sufficiently high (≈900 με). This sensitivity analysis is valid only for the aluminium alloy used here, but similar laboratory-based tests could be performed for other materials to identify the corresponding operating range of the proposed system for crack or damage detection which will be important for the successful deployment of the proposed real-time monitoring system in industrial applications for condition and structural health monitoring.

5. Conclusion

A thermal emissions-based real-time monitoring system has been presented in this study which was designed for *in situ* detection of fatigue cracks in structures under fatigue loading. The proposed system performs crack detection based on the principles of the well-established TSA technique using an IR microbolometer from an OEM. The proposed system costs about 1% of the price of IR photovoltaic effect detector systems typically employed in thermography-based NDE techniques. Proof-of-concept laboratory fatigue tests were performed on open-hole aluminium alloy specimens to compare the performance of the proposed system against a state-of-the-art IR detector system and demonstrate its potential application for crack detection in industrial environments. In these tests, naturally induced fatigue cracks were propagated under two fatigue regimes: (1) constant amplitude cyclic loading and (2) flight cycle loading. IR images acquired from the microbolometer were processed to produce spatial maps of un-calibrated thermoelastic response from a specimen's surface, which are referred to as Condition Assessment using Thermal Emissions (CATE) maps in this paper. CATE maps for each distinct waveform in the fatigue loading sequence were orthogonally decomposed into feature vectors. The Euclidean distance between the feature vectors, representing the CATE maps, were then evaluated and monitored for the automated detection of fatigue cracks. All data processing was performed in quasi real-time on a Raspberry Pi computer, which is comprised of a single board whose footprint is comparable to that of a bank credit card. Traditionally, TSA is perceived as a laboratory-based technique for quantitative fatigue assessment of components under constant amplitude cyclic loading at frequencies greater than 10 Hz. It has been demonstrated that it is possible to detect cracks of the order 1 mm in length in real-time generated by loading waveforms with frequencies as low as 0.3 Hz and to monitor their propagation. This represents a significant advance in improving the feasibility of TSA-based crack detection for use in large-scale structural tests where loading frequencies are often lower than 1 Hz.

Data accessibility. Data on which this study is based are available from the Dryad Digital Repository at: https://doi.org/10.5061/dryad.p8cz8w9rf [35].

The data are provided in electronic supplementary material [36].

Authors' contributions. K.A.: data curation, formal analysis, investigation, methodology, software, visualization, writing—original draft; P.L.: hardware development, data curation, investigation, methodology, software, writing—review and editing; C.A.M.: conceptualization, project administration, writing—review and editing; R.J.G.: conceptualization, funding acquisition, resources, supervision, writing—review and editing; E.A.P.: conceptualization, funding acquisition, project administration, resources, supervision, writing—review and editing.

All authors gave final approval for publication and agreed to be held accountable for the work performed therein.

Conflict of interest declaration. The authors have no competing interests.

Funding. This study was part of the DIMES (Development of Integrated MEasurement Systems) project which has received funding from the Clean Sky 2 Joint Undertaking under the European Union's Horizon 2020 research and innovation programme under grant agreement no. 820951. The opinions expressed in this article reflect only the authors' view and the Clean Sky 2 Joint Undertaking is not responsible for any use that may be made of the information it contains. The University of Liverpool was the coordinator of the DIMES project and the other partners were Empa, Dantec Dynamics GmbH and Strain Solutions Ltd. Airbus was the topic manager on behalf of the Clean Sky 2 Joint Undertaking.

Acknowledgements. The authors acknowledge the productive discussions with their partners and topic manager in the DIMES project, including Erwin Hack of Empa and Linden Harris of Airbus.

References

1. Bagavathiappan S, Lahiri BB, Saravanan T, Philip J, Jayakumar T. 2013 Infrared thermography for condition monitoring: a review. *Infrared Phys. Technol.* **60**, 35–55. (doi:10.1016/j.infrared.2013.03.006)

2. Ciampa F, Mahmoodi P, Pinto F, Meo M. 2018 Recent advances in active infrared thermography for non-destructive testing of aerospace components. *Sensors* **18**, 609. (doi:10.3390/s18020609)
3. Patki A, Patterson EA. 2010 Thermoelastic stress analysis of fatigue cracks subject to overloads. *Fatigue Fract. Eng. Mater. Struct.* **33**, 809–821. (doi:10.1111/j.1460-2695.2010.01471.x)
4. Diaz F, Patterson EA, Tomlinson R, Yates J. 2004 Measuring stress intensity factors during fatigue crack growth using thermoelasticity. *Fatigue Fract. Eng. Mater. Struct.* **27**, 571–583. (doi:10.1111/j.1460-2695.2004.00782.x)
5. Palumbo D, Galietti U. 2014 Characterisation of steel welded joints by infrared thermographic methods. *Quantit. InfraRed Thermogr. J.* **11**, 29–42. (doi:10.1080/17686733.2013.874220)
6. Emery T, Dulieu-Barton J. 2010 Thermoelastic stress analysis of damage mechanisms in composite materials. *Compos. A Appl. Sci. Manufact.* **41**, 1729–1742. (doi:10.1016/j.compositesa.2009.08.015)
7. Krstulovic-Opara L, Klarin B, Neves P, Domazet Z. 2011 Thermal imaging and thermoelastic stress analysis of impact damage of composite materials. *Eng. Fail. Anal.* **18**, 713–719. (doi:10.1016/j.engfailanal.2010.11.010)
8. Shiozawa D, Sakagami T, Nakamura Y, Nonaka S, Hamada K. 2017 Fatigue damage evaluation of short carbon fiber reinforced plastics based on phase information of thermoelastic temperature change. *Sensors* **17**, 2824. (doi:10.3390/s17122824)
9. Pitarresi G, Patterson EA. 2003 A review of the general theory of thermoelastic stress analysis. *J. Strain Anal. Eng. Design* **38**, 405–417. (doi:10.1243/03093240360713469)
10. Stanley P, Chan WK. 1986 'SPATE' stress studies of plates and rings under in-plane loading. *Exp. Mech.* **26**, 360–370. (doi:10.1007/BF02320152)
11. Lesniak JR, Boyce BR. 1994 A high-speed differential thermographic camera. In *Proc. of the SEM Spring Conf. on Experimental Mechanics*, Baltimore, Maryland, pp. 491–499.
12. Palumbo D, Galietti U. 2017 Thermoelastic phase analysis (TPA): a new method for fatigue behaviour analysis of steels. *Fatigue Fract. Eng. Mater. Struct.* **40**, 523–534. (doi:10.1111/ffe.12511)
13. Amjad K, Asquith D, Patterson EA, Sebastian CM, Wang WC. 2017 The interaction of fatigue cracks with a residual stress field using thermoelastic stress analysis and synchrotron X-ray diffraction experiments. *R. Soc. Open Sci.* **4**, 171100. (doi:10.1098/rsos.171100)
14. Tomlinson RA *et al.* 2014 Crack growth study of fibre metal laminates using thermoelastic stress analysis. In *Residual stress, thermomechanics & infrared imaging, hybrid techniques and inverse problems, vol. 8. Conference Proceedings of the society for experimental mechanics series* (ed. M Rossi). Cham: Springer.
15. Palumbo D, De Finis R, Demelio GP, Galietti U. 2017 Study of damage evolution in composite materials based on the thermoelastic phase analysis (TPA) method. *Compos. B Eng.* **117**, 49–60. (doi:10.1016/j.compositesb.2017.02.040)
16. Fruehmann R, Dulieu-Barton J, Quinn S. 2010 Thermoelastic stress and damage analysis using transient loading. *Exp. Mech.* **50**, 1075–1086. (doi:10.1007/s11340-009-9295-9)
17. Rajic N, Street N. 2014 A performance comparison between cooled and uncooled infrared detectors for thermoelastic stress analysis. *Quantit. InfraRed Thermogr. J.* **11**, 207–221. (doi:10.1080/17686733.2014.962835)
18. Rajic N, Rowlands D. 2013 Thermoelastic stress analysis with a compact low-cost microbolometer system. *Quant. InfraRed Thermogr. J.* **10**, 135–158. (doi:10.1080/17686733.2013.800688)
19. Steven BC, Adu-Gyamfi Y. 2016 *Evaluation of fatigue-prone details using a low-cost thermoelastic stress analysis*. Richmond: Virginia Transportation Research Council. Available at: https://rosap.ntl.bts.gov/view/dot/31615.
20. Middleton CA, Weihrauch M, Christian WJR, Greene RJ, Patterson EA. 2020 Detection and tracking of cracks based on thermoelastic stress analysis. *R. Soc. Open Sci.* **7**, 200823. (doi:10.1098/rsos.200823)
21. Fruehmann RK, Dulieu-Barton JM, Quinn S, Peton-Walter J, Mousty PAN. 2012 The application of thermoelastic stress analysis to full-scale aerospace structures. *J. Phys: Conf. Ser.* **382**, 012058. IOP Publishing. (doi:10.1088/1742-6596/382/1/012058)
22. Tomlinson RA, Patterson EA. 2011 Examination of crack tip plasticity using thermoelastic stress analysis. In *Thermomechanics and infra-red imaging, volume 7. Conference Proceedings of the society for experimental mechanics series*. New York, NY Berlin, Germany: Springer.

23. Robinson A, Dulieu-Barton J, Quinn S, Burguete R. 2009 A review of residual stress analysis using thermoelastic techniques. In: *Journal of Physics: Conference Series*, vol. 181, 7th Int. Conf. on Modern Practice in Stress and Vibration Analysis. IOP publishing, Bristol, UK.
24. Palumbo D, Galietti U. 2016 Data correction for thermoelastic stress analysis on titanium components. *Exp. Mech.* **56**, 451–462. (doi:10.1007/s11340-015-0115-0)
25. Solomon C, Breckon T. 2011 *Fundamentals of digital image processing: A practical approach with examples in Matlab*. Chichester, UK: John Wiley & Sons.
26. Mukundan R, Ong S, Lee PA. 2001 Image analysis by Tchebichef moments. *IEEE Trans. Image Process.* **10**, 1357–1364. (doi:10.1109/83.941859)
27. Yap PT, Paramesran R, Ong SH. 2007 Image analysis using Hahn moments. *IEEE Trans. Pattern Anal. Mach. Intell.* **29**, 2057–2062. (doi:10.1109/TPAMI.2007.70709)
28. Sebastian CM, Hack E, Patterson EA. 2013 An approach to the validation of computational solid mechanics models for strain analysis. *J. Strain Anal. Eng. Design* **48**, 36–47. (doi:10.1177/0309324712453409)
29. Christian WJR, Dvurecenska K, Amjad K, Pierce J, Przybyla C, Patterson EA. 2020 Real-time quantification of damage in structural materials during mechanical testing. *R. Soc. Open Sci.* **7**, 191407. (doi:10.1098/rsos.191407)
30. Huber PJ. 2004 *Robust statistics*. Hoboken, NJ: John Wiley & Sons.
31. Rajic N, Street N, Brooks C, Galea S. 2014 Full Field Stress Measurement for in Situ Structural Health Monitoring of Airframe Components and Repairs. In *EWSHM - 7th European Workshop on Structural Health Monitoring*. IFFSTTAR, Inria, Université de Nantes, Nantes, France. hal-01020305.
32. Rajic N, Brooks C. 2017 Automated crack detection and crack growth rate measurement using thermoelasticity. *Procedia Eng.* **188**, 463–470. (doi:10.1016/j.proeng.2017.04.509)
33. Middleton CA, Gaio A, Greene R, Patterson EA. 2019 Towards automated tracking of initiation and propagation of cracks in aluminium alloy coupons using thermoelastic stress analysis. *J. Nondestr. Eval.* **38**, 18. (doi:10.1007/s10921-018-0555-4)
34. Thatcher JE, Crump DA, Devivier C, Bailey PBS, Dulieu-Barton JM. 2020 Low cost infrared thermography for automated crack monitoring in fatigue testing. *Opt. Lasers Eng.* **126**, 105914. (doi:10.1016/j.optlaseng.2019.105914)
35. Amjad K, Lambert P, Middleton CA, Greene RJ, Patterson EA. 2022 Data from: A thermal emissions-based real-time monitoring system for in situ detection of fatigue cracks. Dryad Digital Repository. (doi:10.5061/dryad.p8cz8w9rf)
36. Amjad K, Lambert P, Middleton CA, Greene RJ, Patterson EA. 2022 A thermal emissions-based real-time monitoring system for *in situ* detection of fatigue cracks. Figshare. (doi:10.6084/m9.figshare.c.6214714)